



RESEARCH ARTICLE

Tropical tropospheric warming pattern explained by shifts in convective heating in the Matsuno–Gill model

P. Keil^{1,2}  | H. Schmidt¹ | B. Stevens¹  | M. P. Byrne^{3,4}  | H. Segura¹ | D. Putrasahan¹¹Max Planck Institute for Meteorology, Hamburg, Germany²International Max Planck Research School on Earth System Modelling, Hamburg, Germany³School of Earth and Environmental Sciences, University of St Andrews, St Andrews, UK⁴Department of Physics, University of Oxford, Oxford, UK**Correspondence**

P. Keil, Max Planck Institute for Meteorology, Bundesstraße 53, 20146 Hamburg, Germany.

Email: paul.keil@mpimet.mpg.de and keil@dkrz.de**Funding information**

German Federal Ministry of Education and Research; Max-Planck-Gesellschaft

Abstract

Horizontal temperature gradients in the tropical free troposphere are fairly weak, and tropical tropospheric warming is usually treated as uniform. However, we show here that projected tropospheric warming is spatially inhomogeneous in Coupled Model Intercomparison Project Phase 6 models, as well as in a storm-resolving climate model. We relate the upper tropospheric warming pattern to sea-surface temperature changes that reorganise convection and thereby cause spatial shifts in convective heating. Using the classical Gill model for tropical circulation and forcing it with precipitation changes that arise due to greenhouse gas warming, we can understand and reproduce the different warming patterns simulated by a range of global climate models. Forcing the Gill model with precipitation changes from a certain region demonstrates how local tropospheric temperature changes depend on local changes in convective heating. Close to the Equator, anomalous geopotential gradients are balanced by the dissipation term in the Gill model. The optimal dissipation time-scale to reproduce the warming pattern varies depending on the Coupled Model Intercomparison Project Phase 6 model, and is between 1 and 10 days. We demonstrate that horizontal advection and eddy momentum fluxes have large enough equivalent dissipation time-scales to balance the gradients in geopotential and thereby shape the warming pattern. Though climate models show a large spread in projections of tropical sea-surface temperature and precipitation changes, our results imply that, once these predictions improve, our confidence in the predicted upper tropospheric warming pattern should also increase.

KEYWORDS

climate change, convection, simple models, tropical circulation, tropospheric warming

1 | INTRODUCTION

In the tropical free troposphere, horizontal buoyancy gradients produced by deep convection are quickly reduced by gravity waves due to the absence of a strong Coriolis

force (Bretherton and Smolarkiewicz, 1989), resulting in weak geopotential gradients. Thus, the temperature throughout the tropical free troposphere is approximately horizontally uniform and set by the temperature and moisture in the boundary layer of the convecting

regions (Emanuel *et al.*, 1994). Consequently, in a warming climate, increased boundary-layer temperatures lead to approximately horizontally homogeneous warming throughout the tropical free troposphere. This warming is amplified with respect to the boundary layer since the warmer air can hold additional water vapour, and thus additional latent heating occurs in the free tropical troposphere, which changes the steepness of the moist adiabatic lapse rate (Santer *et al.*, 2005). Though climate models continue to show biases in various aspects of tropical climate, maybe most striking for precipitation (Fiedler *et al.*, 2020), estimates of horizontal mean upper tropospheric warming are arguably within the range of measurement errors and internal variability (Santer *et al.*, 2017; Po-Chedley *et al.*, 2021).

The small gradients in geopotential and temperature are exploited in the weak temperature gradient (WTG) approximation (Sobel and Bretherton, 2000; Sobel *et al.*, 2001), which is both conceptually powerful and useful for many applications (e.g., Bretherton and Sobel (2002)). Nevertheless, horizontal temperature gradients of several degrees kelvin do exist in the free tropical troposphere. These temperature gradients persist over months and develop in response to strong local convective heating; for example, during the Indian summer monsoon (Wu *et al.*, 2015) and in response to the El Niño–Southern Oscillation (Bayr *et al.*, 2014). In the lower tropical troposphere, horizontal temperature gradients are weak and mostly related to the impact of water vapour and condensate on the air's density (Yang *et al.*, 2022), but temperature gradients in the tropical upper troposphere are substantial and cannot be explained by this effect (Bao and Stevens, 2021). Observed recent tropospheric warming is also inhomogeneous, and possibly linked to sea-surface temperature (SST) patterns (Kamae *et al.*, 2015), which in turn organise convection (Lindzen and Nigam, 1987). In addition, we find that, in climate simulations under greenhouse gas forcing, upper tropospheric warming shows deviations of more than 2 K from region to region in most Coupled Model Intercomparison Project phase 6 (CMIP6; (Eyring *et al.*, 2016)) models. The pattern differs among the models, resulting in a more uniform ensemble mean upper tropospheric warming pattern, with deviations of less than 1 K (Figure 1a). We also examine upper tropospheric warming in two simulations forced by boundary conditions from a cold and warm climate using a storm-resolving model that represents convection explicitly through the laws of motion and not through a parametrisation that includes empirical assumptions (Stevens *et al.*, 2020). The difference between the warm and cold simulations reveals that tropical upper tropospheric warming also differs by up to 2 K horizontally (Figure 1b). Horizontal differences in tropospheric

warming have implications for how observed warming is sampled by sparsely distributed radiosonde stations and, by impacting upper tropospheric static stability, could be an important influence on tropical circulation systems like the Pacific Walker circulation (Sohn *et al.*, 2016) and on tropical cyclone intensity (Trabing *et al.*, 2019). Though the SST pattern seems to play an important role (Kamae *et al.*, 2015), likely by impacting deep convection, what mechanisms exactly govern the upper tropospheric warming pattern are unclear.

Here, we use the Matsuno–Webster–Gill model (Matsuno, 1966; Webster, 1972; Gill, 1980), from now on referred to as the Gill model, for tropical circulation to understand the pattern of tropospheric warming. Though the Gill model cannot capture the full dynamics of the tropical atmosphere, especially at smaller spatial and temporal scales, it has proven very useful to describe the large-scale tropical circulation and geopotential characteristics (Gill, 1980; Lau and Lim, 1982; Dias *et al.*, 1983; Rodwell and Hoskins, 1996; Lin *et al.*, 2008; Shaw and Boos, 2012). We show that the warming pattern is related to horizontal changes in convection by only using precipitation to force the Gill model and thereby reproduce these patterns. Besides the pressure gradient force and Coriolis force, it includes a dissipation term that can be understood as a contribution from more complicated, nonlinear processes such as advection and convective momentum transport in the momentum equations (Sardeshmukh and Held, 1984; Lin *et al.*, 2008), as well as radiative cooling. Although the magnitudes of these processes are typically small compared with, for example, the Coriolis force in the extratropics, they are essential to balance the geopotential gradients close to the Equator (Bao *et al.*, 2022). We will show that this dissipation term is essential to understand and reproduce the tropospheric warming pattern.

Section 2 describes the methods, including the global climate model data and the implementation of the Gill model. Section 3 documents the spatial anomalies in surface warming and upper tropospheric warming in different global climate models and shows the mechanisms behind precipitation and convective heating changes. In Section 4 we demonstrate how the Gill model can reproduce large-scale changes in upper tropospheric temperatures using the changes in precipitation as forcing and discuss the dependence of the results on the dissipation term. The method is also applied to reproduce warming patterns in the vast majority of CMIP6 models. We use these results to determine the most skilful values for the dissipation term to reproduce the warming pattern, which elucidates what processes are likely represented by the dissipation term. Section 5 contains a conclusion and further points of discussion.

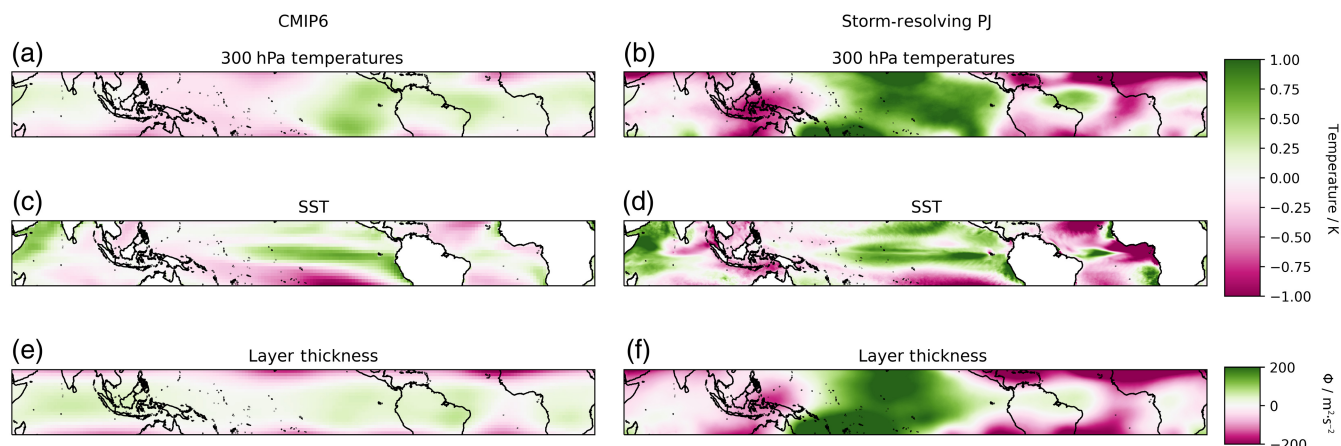


FIGURE 1 Anomalies from tropical mean (20° N– 20° S) changes in January between the early (2015–2034) and late (2088–2099) period in Coupled Model Intercomparison Project phase 6 (CMIP6) SSP585 models and the warm and cold simulations in the storm-resolving perpetual January (PJ) simulations: (a, b) temperatures at 300 hPa; (c, d) sea-surface temperatures (SSTs); (e, f), 400–150 hPa layer thickness. [Colour figure can be viewed at [wileyonlinelibrary.com](https://onlinelibrary.wiley.com)]

2 | METHODS

2.1 | Climate models

2.1.1 | Perpetual January

We analyse upper tropospheric warming patterns, layer thickness changes, and precipitation changes in two so-called perpetual January (PJ) simulations. These simulations are performed with the ICON-A model at a storm-resolving horizontal resolution (5 km) and thus do not rely on convection and gravity-wave parametrisations (Hohenegger *et al.*, 2022), thereby improving many aspects of the simulated tropical climate in comparison with conventional climate models (Stevens *et al.*, 2020). Since the computational cost of these simulations is quite high, two simulations with eight months each are analysed, both using only January boundary conditions for all months (hence the term PJ). SSTs and sea-ice boundary conditions are taken from simulations with the Max Planck Institute Earth System Model employing an eddy-resolving component (MPI-ESM-ER) that use approximately 10 km resolution in the ocean model and 1° in the atmosphere (Gutjahr *et al.*, 2019). Thereby, the SST frontal regions and their effect on the atmosphere are fully captured. One PJ simulation uses boundary conditions averaged over 40 Januaries from an MPI-ESM-ER control simulation with greenhouse gas levels set to those of the year 1950, whereas the other uses the average over 40 Januaries from two ensemble members from the time period 2080–2099 using the SSP585 scenario in the MPI-ESM-ER model (Putrasahan *et al.*, 2021). MPI-ESM-ER was chosen because it is one of the few global coupled models with an eddy-resolving ocean for which such simulations exist. Throughout the

study we present temperature, layer thickness, and precipitation changes as differences between the warm and the cold simulation.

2.1.2 | CMIP6

We also present upper tropospheric warming patterns and layer thickness changes in the simulations driven by the SSP585 emission scenario (O'Neill *et al.*, 2016) performed by those 31 CMIP6 models (Eyring *et al.*, 2016) that provide all required data for this experiment. The SSP585 scenario represents a scenario with high greenhouse gas emissions, and therefore these experiments show strong global warming. We analyse one ensemble member (“r1i1p1f1”) for every model and show differences between the late (2080–2099) and early 21st century (2015–2034).

2.2 | Numerical Gill model

To understand the warming pattern produced in the climate models and identify the relevant processes, we employ the Gill model that can reproduce the large-scale characteristics of the tropical circulation (Matsuno, 1966; Webster, 1972; Gill, 1980). The equations were first derived and their general wave-like solutions presented by Matsuno (1966), and the first numerical solutions to a steady forcing were investigated by Webster (1972). It was Gill's elegant analytic solutions that made the steady-state behaviour of the equations – something we approximate by integrating under steady forcing (constant in time) – first clearly apparent. We use the linearised shallow-water equations on the equatorial β -plane including a stationary

forcing $Q(x, y)$ in the combined thermodynamic and continuity equation as a starting point (e.g., Matsuno (1966)):

$$\begin{aligned} \frac{\partial u}{\partial t} - \beta y v &= -\frac{\partial \Phi}{\partial x}, \\ \frac{\partial v}{\partial t} + \beta y u &= -\frac{\partial \Phi}{\partial y}, \\ \frac{\partial \Phi}{\partial t} + \alpha \left(\frac{\partial u}{\partial x} + \frac{\partial v}{\partial y} \right) &= Q. \end{aligned} \quad (1)$$

Typically, Φ is geopotential height, u and v are zonal and meridional wind velocities, and β is the Rossby parameter for the β -plane approximation, but we interpret these equations slightly differently. Here, u and v are the differences in zonal and meridional winds between the upper layer (in this case 150 hPa) and lower layer (in this case 400 hPa), and Φ is the geopotential deviation from a reference layer thickness – for example, see discussion in Matsuno (1966). We use these pressure levels since the bulk of the additional warming due to the release of condensation heating is realised in the upper troposphere (Figure 2), but we also discuss other choices throughout the text. Thus, Φ can be interpreted as a layer thickness proportional to upper tropospheric temperatures in this layer. Then, $\alpha = Sa$, where S , the static stability, is given by

$$S = \frac{\partial \bar{\Phi}}{\partial p} \frac{\partial \log(\theta)}{\partial p},$$

in which $\bar{\Phi}$ and θ are respectively the average geopotential and the potential temperature of the chosen layer, and a is a parameter related to the chosen vertical levels. For typical values using the 750–250 hPa layer, which is perhaps the most common use case, $\alpha \approx 4,500 \text{ m}^2 \cdot \text{s}^{-2}$, which is equivalent to the values used by Gill (1980). Here, we are mostly interested in the tropical upper troposphere, and therefore mostly use values for the 400–150 hPa layer, resulting in $\alpha \approx 2,800 \text{ m}^2 \cdot \text{s}^{-2}$. α can be interpreted as $\alpha = gH$, where H is an effective layer thickness and g is the gravitational constant, and also determines the gravity wave speed (Matsuno, 1966; Gill, 1980).

The geopotential source Q can be related to thermal heating rate \bar{Q} ($\text{K} \cdot \text{s}^{-1}$):

$$Q = R\bar{Q} \ln\left(\frac{p_b}{p_t}\right), \quad (2)$$

where R is the gas constant and p_t and p_b are the upper and lower pressure layers respectively. See the Appendix for a complete derivation of the thermodynamic equation.

Following Gill (1980), the chosen length scale is

$$L = \sqrt{\frac{\sqrt{\alpha}}{2\beta}}, \quad (3)$$

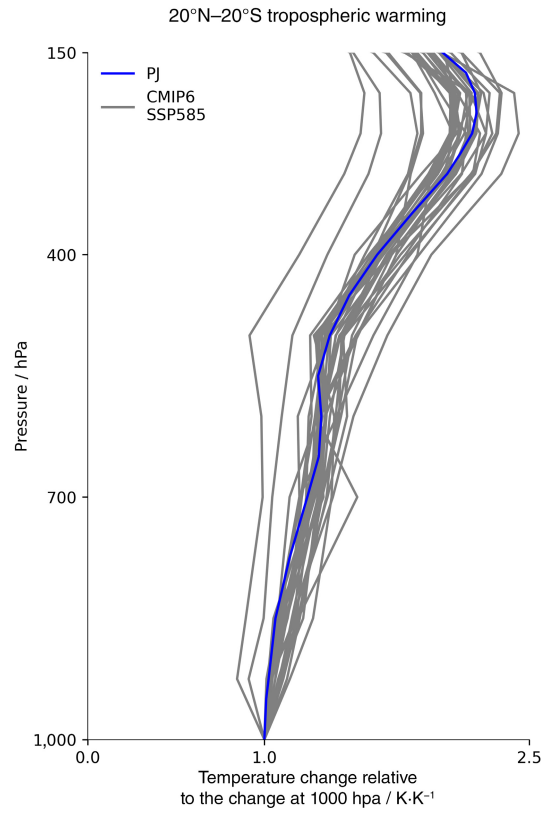


FIGURE 2 Ratio of tropical mean (20° N–20° S) temperature change at different pressure levels and the 1,000 hPa temperature change in January in CMIP6 models and perpetual January (PJ) simulations. Changes are calculated as the difference between the early and late period in CMIP6 SSP585 models (grey) and the warm and cold PJ simulation (blue). [Colour figure can be viewed at wileyonlinelibrary.com]

corresponding to about 10° of latitude, which is roughly the tropical deformation radius, and the chosen time-scale is

$$T = \sqrt{\frac{1}{2\sqrt{\alpha\beta}}}, \quad (4)$$

corresponding to about 6 hr, which is roughly the time-scale during which deep convective clouds form (Hohenegger and Stevens, 2013). Even though the estimate used for α is somewhat different, the resulting values for L and T are very similar to the ones used in Gill (1980). Now, the equations can be non-dimensionalised and the dissipation terms $\epsilon_w u$, $\epsilon_w v$, and $\epsilon_p \Phi$ are introduced:

$$\begin{aligned} \frac{\partial u}{\partial t} + \epsilon_w u - \frac{1}{2} y v &= -\frac{\partial \Phi}{\partial x}, \\ \frac{\partial v}{\partial t} + \epsilon_w v + \frac{1}{2} y u &= -\frac{\partial \Phi}{\partial y}, \\ \frac{\partial \Phi}{\partial t} + \epsilon_p \Phi + \frac{\partial u}{\partial x} + \frac{\partial v}{\partial y} &= Q. \end{aligned} \quad (5)$$

From here on, all symbols represent dimensionless quantities. The momentum dissipation terms $\epsilon_w u$ and $\epsilon_w v$ parametrise additional, more complex processes, like advection or eddy momentum fluxes (Lin *et al.*, 2008), and the Newtonian cooling $\epsilon_p \Phi$ mimics radiative cooling. Unlike Matsuno (1966) and Gill (1980), we distinguish between the momentum and the thermal dissipation parameters ϵ_p and ϵ_w , because the underlying processes are different. When we refer to ϵ throughout the article, this includes both ϵ_p and ϵ_w . Note that the inverse of ϵ can be interpreted as a dissipation time-scale.

We use the model in Equation (5) in numerical form, discretised with first-order centred differences in space and a Runge–Kutta integrator in time on a $2^\circ \times 2^\circ$ grid from 30° N to 30° S. The model is integrated in time until a steady state is reached. We employ this method because it is fairly simple and sufficiently fast, although we recognise that solving the steady-state problem directly might be less prone to numerical errors. We use the threshold $\Phi(t+1) - \Phi(t) < 10^{-5} \alpha = 0.28 \text{ m}^2 \cdot \text{s}^{-2}$ at all grid points as a convergence criterion. The thermal heating rate \bar{Q} is time independent and derived from the precipitation changes in global climate models that are interpolated to the $2^\circ \times 2^\circ$ grid, assuming that all condensation leads to precipitation (Gill, 1982):

$$\bar{Q}(x, y) = \frac{L_v P(x, y)}{\rho c_p h} = -\frac{L_v P(x, y)}{c_p h} \frac{\partial \bar{\Phi}}{\partial p}, \quad (6)$$

where L_v is the latent heat of vaporisation, ρ is typical midtropospheric density, which is related to the vertical gradient in geopotential $\partial \bar{\Phi} / \partial p = -1/\rho \approx -2.6 \text{ m}^2 \cdot \text{s}^{-2} \cdot \text{Pa}^{-1}$ for the 400–150 hPa layer, c_p is the specific heat capacity of dry air, and $h = 6,500 \text{ m}$ is the height over which the heating is distributed (the approximate height difference between 400 and 150 hPa). These values are constant throughout the domain. Here, we have also assumed that all of the temperature anomalies that arise due to convective heating anomalies are realised in this layer, because the bulk of the heating is realised in this layer (Figure 2). The precipitation changes P on the $2^\circ \times 2^\circ$ grid are smoothed by retaining the first 100 (out of 180) wave numbers (in spectral space) in the x -direction and first 16 (out of 30) wave numbers in the y -direction. This does not affect the results qualitatively or hardly quantitatively, but serves to reduce the noise in the solution that arises due to strong gradients at some regions in the forcing.

If not stated otherwise, P is the change in precipitation between a warm and a cold climate simulated by different global climate models. This means that u , v , and Φ also represent the changes between the two climates. Assuming ϵ and α do not change with warming, all terms in the Gill model are linear, and therefore this approach is equivalent

to simulating the warm and cold climates explicitly with the Gill model and then taking the difference between these simulations. In Section 4.3 we examine the validity of this assumption. Simulations with the Gill model using the latent heating rates from phase changes calculated by the microphysical scheme in the PJ simulations instead of precipitation yield similar results and, therefore, are not discussed.

3 | TROPICAL TROPOSPHERIC WARMING PATTERNS AND PRECIPITATION CHANGES IN GLOBAL CLIMATE MODELS

In CMIP6 simulations, the warming in the tropical upper troposphere is amplified with respect to the surface (Figure 2) and at first glance is broadly horizontally uniform (Figure 1a), especially compared with higher latitudes. However, the CMIP6 models show a stronger warming in the eastern Pacific compared with the rest of the Tropics in the multimodel ensemble mean (Figure 1a). Most individual models show considerably stronger deviations, in many cases more than 2 K horizontal difference between the regions of strongest and weakest warming, and the regional patterns differ from model to model. The storm-resolving PJ simulations (Figure 1b) show horizontal anomalies from the mean tropospheric warming of a similar magnitude to the individual CMIP6 models, with the strongest warming in the western Pacific. For example, the warming in the western Pacific, south of the Equator, is around 2 K stronger than the warming over the neighbouring Maritime Continent. This anomalous warming is also reflected in the geopotential layer thickness

$$\bar{\Phi} = \int \frac{R T_v}{p} dp, \quad (7)$$

where T_v is the virtual temperature and p is pressure. The 400 to 150 hPa layer thickness (Figure 1e,f) shows very similar patterns to the 300 hPa temperatures. Generally, in regions where the layer thickness increases above average, upper tropospheric warming is also above average. The layer thickness changes in the CMIP6 models are more longitudinally uniform compared with the temperature pattern. Upper tropospheric layer thickness anomalies and SST anomalies regionally coincide to some degree (Figure 1c,d), similar to the case of the recently observed temperature anomalies in the Pacific (Kamae *et al.*, 2015). However, the correlation between SST anomalies and upper tropospheric temperature anomalies at 20° N– 20° S is only at 0.4 in the PJ simulations and on average 0.2 in the CMIP6 simulations, with a maximum value

of 0.5. The strong warming over land surfaces (not shown) does not translate into stronger upper tropospheric warming. Similar to the upper tropospheric warming pattern, the SST pattern varies considerably among CMIP6 models.

The most likely mechanism by which SST anomalies and upper tropospheric temperatures are connected is through deep convection, which releases latent heat in the troposphere. Indeed, changes in precipitation (Figure 3a) seem to roughly resemble the SST warming pattern (Figure 1d). The changes in precipitation in CMIP6 models vary, and the ensemble mean is considerably different compared with the PJ simulations (not shown). An increase in precipitation could be related to an increase of humidity that occurs due to the warmer SSTs, and is transported by the mean circulation to the regions of deep convection. This can be characterised as thermodynamic changes in convection (Held and Soden, 2006). Alternatively, precipitation changes could be related to dynamic changes triggered by the SST pattern (Lindzen and Nigam, 1987), where an increase in moisture convergence would be associated with an increase of horizontal convergence of the winds or increased moisture advection. To understand which of these processes is more important we adopt the methodology of Seager *et al.* (2010) to decompose the precipitation changes into components that are driven by thermodynamic, dynamic, and residual terms. Recently, it has been demonstrated that the dynamic components dominate the other components in CMIP6 models (Elbaum *et al.*, 2022), and here we want to confirm this result in a storm-resolving model. The changes in precipitation ΔP are related to changes in the mass-weighted vertically integrated moisture flux convergence and changes in evaporation ΔE :

$$\Delta P = \Delta E - \Delta \int_{p=p_s}^{p=0} \nabla \cdot (\mathbf{U}q) \frac{dp}{g}, \quad (8)$$

where \mathbf{U} is the horizontal wind vector, q is specific humidity, and g is the gravitational acceleration. Δ denotes differences between the warm and cold PJ simulations. The mass-weighted integral on the right-hand side quantifies the change in atmospheric moisture convergence between the simulations. The dynamic changes are related to changes in the winds $\Delta \mathbf{U}$:

$$\Delta P_{\text{dyn}} = - \int_{p=p_s}^{p=0} \nabla \cdot (\Delta \mathbf{U} q) \frac{dp}{g}, \quad (9)$$

whereas the thermodynamic changes are related to changes in the specific humidity Δq :

$$\Delta P_{\text{th}} = - \int_{p=p_s}^{p=0} \nabla \cdot (\mathbf{U} \Delta q) \frac{dp}{g}. \quad (10)$$

All the aforementioned terms are calculated with monthly mean data. The residual ΔP_{res} is given by

$$\Delta P_{\text{res}} = \Delta P - \Delta E - \Delta P_{\text{th}} - \Delta P_{\text{dyn}} \quad (11)$$

and includes contributions from transient eddies and other processes (Seager *et al.*, 2010).

In the PJ simulations, ΔP_{dyn} dominates the other terms (Figure 3). The most prominent precipitation changes, such as the strong increase east of Australia and the distinctive pattern in the Atlantic, are reflected in ΔP_{dyn} . The thermodynamic changes ΔP_{th} are typically smaller in magnitude and mostly opposed to the dynamic changes, which agrees with earlier results (Seager *et al.*, 2010; Bony *et al.*, 2013; Elbaum *et al.*, 2022). Over land, the thermodynamic changes ΔP_{th} are slightly stronger than the dynamic changes ΔP_{dyn} , likely because the availability of moisture plays a larger role compared with over oceans. The residual ΔP_{res} is not negligible, but smaller than ΔP_{dyn} and ΔP_{th} . We conclude that precipitation changes in the PJ simulations are coupled to circulation changes. Note that there is no monocausal relationship in which a change in one causes a change in the other, but not vice versa.

Thus, the SST warming pattern triggers shifts in convective activity and thereby changes circulation and precipitation. If upper tropospheric warming is indeed related to the changes of convective heating, as the next section will demonstrate, then the upper tropospheric warming pattern does not follow a simple thermodynamic argument but is coupled to circulation changes.

4 | INTERPRETING THE WARMING PATTERN USING THE GILL MODEL

This section compares the layer thickness pattern produced by the Gill model with the layer thickness anomalies in the global climate models. The Gill model produces a non-dimensionalised layer thickness, which we present redimensionalised (i.e., multiplied by $\alpha = 2,800 \text{ m}^2 \cdot \text{s}^{-2}$) and compare with the 400–150 hPa layer thickness anomalies in the global climate models. We discuss this choice and compare other layers briefly in Section 4.1. Since it is not clear what value ϵ should have, we perform an ensemble of Gill simulations with different combinations of ϵ_p and ϵ_w . We only use those Gill simulations that converge to a steady state, which is usually the case for sufficiently large ϵ . The numerical Gill model implemented here can reproduce the analytical solutions of Gill (1980) accurately; for example, the response to asymmetrical forcing (Figure 4). Positive forcing (heating) induces an increase in layer thickness north of the Equator, which extends to the

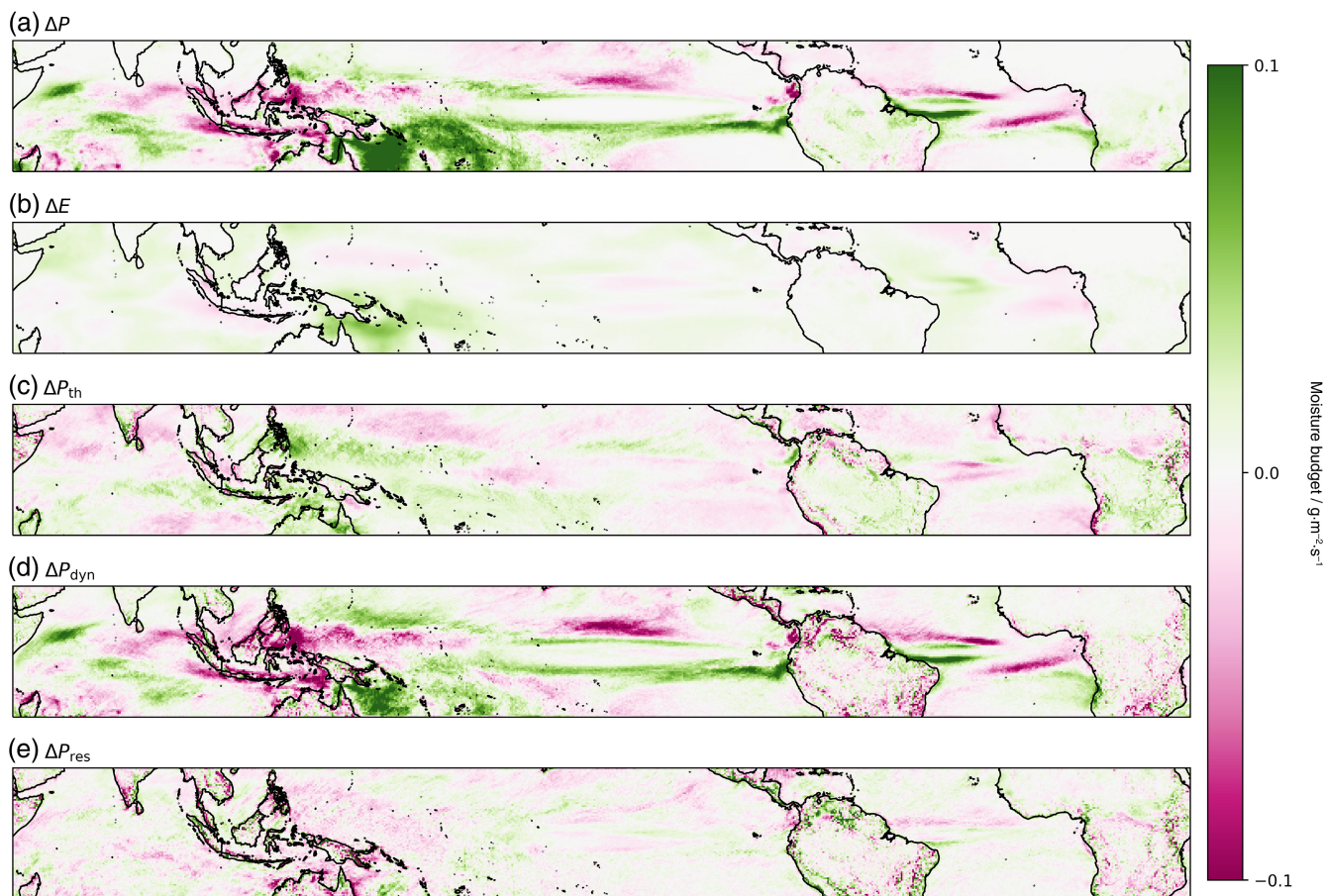


FIGURE 3 Precipitation changes ΔP in (a) the perpetual January simulations decomposed into (c) thermodynamic (ΔP_{th}) and (d) dynamic (ΔP_{dyn}) changes. (b) Evaporation changes ΔE . (e) The residual ΔP_{res} . The signs are such that they are positive for atmospheric moisture loss for all terms (positive values correspond to increased rainfall), except for ΔE , where positive values indicate atmospheric moisture gain. [Colour figure can be viewed at wileyonlinelibrary.com]

west as a Rossby wave and to the east along the Equator as a Kelvin wave.

As demonstrated in the previous section, the convective heating changes are connected to circulation changes in the PJ simulations. This is also the case in the CMIP6 models (Elbaum *et al.*, 2022). This coupling of convective heating and circulation is also represented in the Gill model, as a positive convective heating is balanced by convergence in the lower layer and divergence in the upper layer. Therefore, the Gill model should be suited to reproduce the warming pattern and underlying processes.

4.1 | Storm-resolving PJ simulations

Having verified our implementation of the model against the analytic solutions, we now present layer thickness anomalies produced by Gill simulations forced with the PJ precipitation changes for different values of ϵ (Figure 5). The Gill model layer thickness has a broadly similar

magnitude to the layer thickness anomalies in the PJ simulations, suggesting that the behaviour is well described by the balances retained in the Gill model. The magnitude depends on the forcing amplitude Q , which in turn depends on several assumptions, Equation (2), as well as the values used for ϵ . In contrast, the shape of the pattern primarily depends on ϵ . Given this uncertainty for the magnitude, we focus primarily on how well the spatial patterns match. In all Gill simulations, the strong increase in layer thickness east of Australia, where the precipitation changes are most pronounced, is reproduced. The below-average tropospheric warming over the Maritime Continent is also captured well. For $\epsilon = 0.2$ the layer thickness perturbation across large parts of the Pacific resembles the PJ layer thickness changes closely. For stronger dissipation ($\epsilon = 1.2$), the layer thickness perturbations are more localised and less smeared out. This results in a less realistic pattern in the eastern Pacific, but other, more small-scale features of the warming patterns can be reproduced, such as the small patch of above-average warming

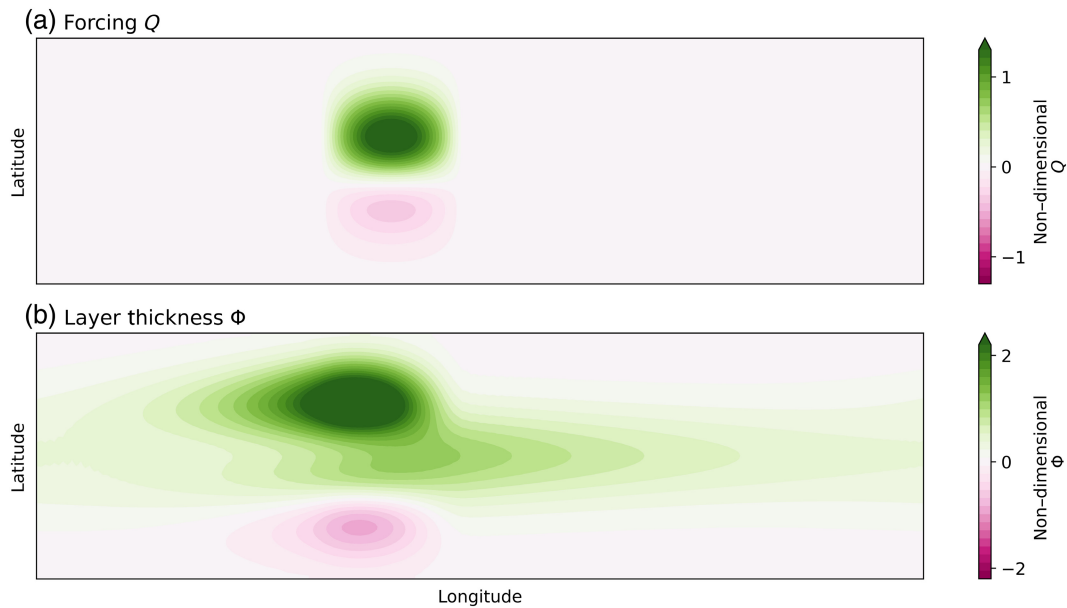


FIGURE 4 (a) Idealised asymmetric forcing and (b) the corresponding layer thickness solution produced by the numerical Gill model. For this idealised forcing there are analytical solutions (Gill, 1980). Positive forcing induces positive tropospheric layer thickness changes, corresponding to negative surface pressure anomalies in other interpretations of the Gill model (Gill, 1980). [Colour figure can be viewed at wileyonlinelibrary.com]

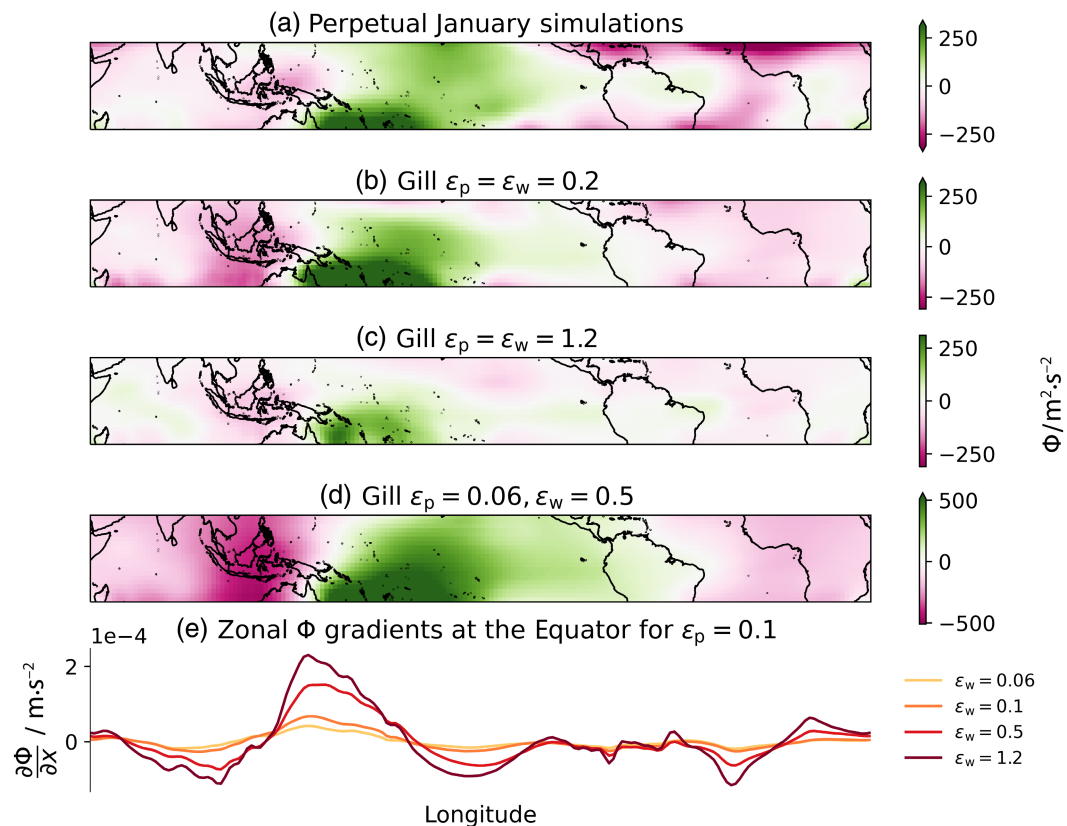
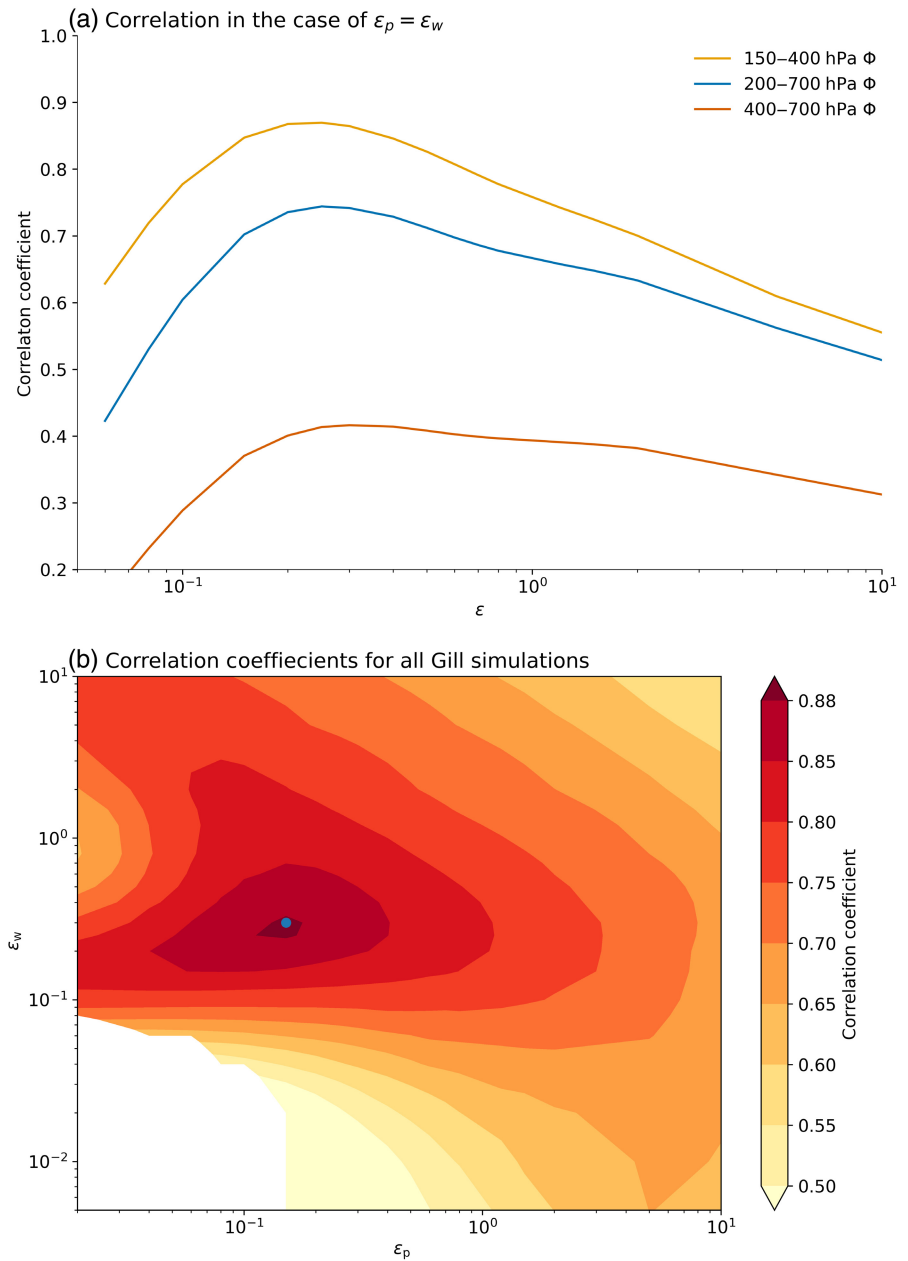


FIGURE 5 Anomalies from (a) the tropical (20° N– 20° S) average layer thickness changes from the perpetual January simulation (as Figure 1e) and (b–d) the tropical (20° N– 20° S) average layer thickness produced by the Gill model forced by the perpetual January precipitation changes. (e) Zonal layer thickness gradients for different Gill simulations at the Equator. [Colour figure can be viewed at wileyonlinelibrary.com]

FIGURE 6 Correlation coefficient between the perpetual January (PJ) layer thickness and Gill simulations forced by precipitation changes. (a) Correlation between 700–200, 400–150, and 700–400 hPa layer thickness changes in the PJ simulation and the Gill simulation for the case of $\epsilon_p = \epsilon_w$. (b) Correlation coefficients between PJ 400–150 hPa layer thickness changes and the Gill simulation for all combinations of ϵ_p and ϵ_w . White space denotes simulations that did not converge and thus are not considered. Correlations are calculated from 20° S to 10° N, since the Northern Hemisphere is the winter hemisphere. The blue dot denotes the values for which the correlation is highest. [Colour figure can be viewed at wileyonlinelibrary.com]



in the equatorial western Atlantic. For a small ϵ_p but larger ϵ_w (Figure 5d), the widespread Pacific warming and the below-average warming over the Maritime Continent are reproduced well, but features on smaller scales are less well represented. Overall, the numerical Gill model can reproduce the strong Pacific warming and the weak Maritime Continent warming well, as well as some of the more local warming patches for larger dissipation.

The dissipation terms have a considerable influence on the pattern. A large thermal dissipation $\epsilon_p \Phi$ balances the convective heating Q in the thermodynamic equation, and therefore the layer thickness pattern Φ will tend to resemble the pattern of convective heating Q for the case of large ϵ_p . Thus, ϵ_p controls how far a signal can travel before it

dissipates. The momentum dissipation $\epsilon_w u$ can help sustain strong zonal gradients of Φ even close to the Equator, which can be seen qualitatively in Figure 5d, which shows a case of large ϵ_w . Larger values for ϵ_w are associated with larger layer thickness gradients along the Equator at all longitudes (Figure 5e), inhibiting the homogenisation of the layer thickness anomalies through gravity waves. Therefore, one can also think of the dissipation terms as determining a basin of influence for a given convective forcing.

We evaluate the performance of the Gill model in explaining the behaviour of the PJ simulations more quantitatively by calculating the Pearson correlation coefficients between the layer thickness patterns (Figure 6). In

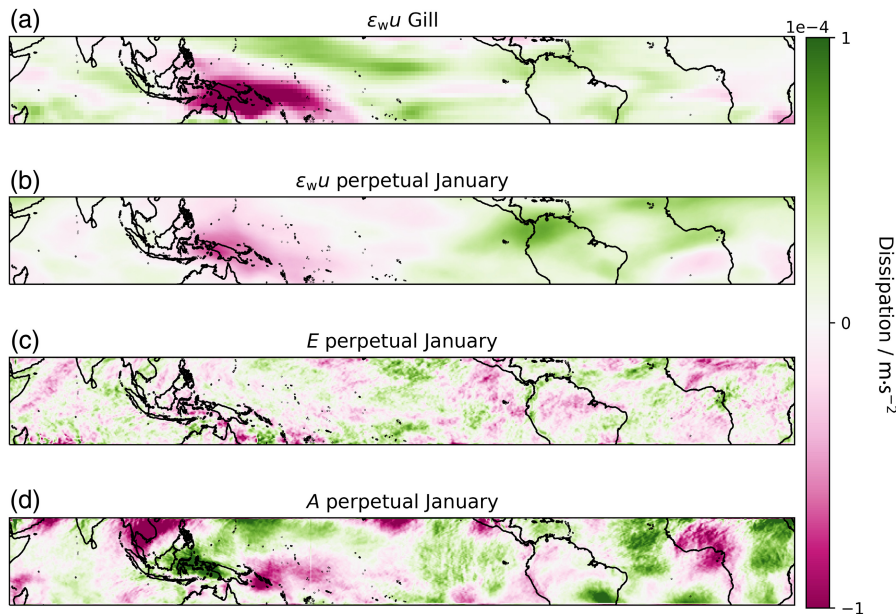


FIGURE 7 Zonal momentum dissipation and its equivalent processes. (a) Redimensionalised zonal momentum dissipation in the Gill simulation. (b) Zonal momentum dissipation calculated from the changes in zonal wind shear between the 400 hPa and the 150 hPa layer in the PJ simulations. (c) Changes in the horizontal eddy momentum fluxes E in the PJ simulations. (d) Changes in horizontal advection A in the PJ simulations. Panels (a) and (b) show momentum dissipation for $\epsilon_w = 0.1$, which is equivalent to the dimensional dissipation time-scale of 2 days. A and E are shown as the difference between the 150 and 400 hPa layers. [Colour figure can be viewed at wileyonlinelibrary.com]

the case of $\epsilon_p = \epsilon_w$ (Figure 6a), the Gill simulations perform best for ϵ between 0.2 and 0.3; indeed, the simulation with $\epsilon = 0.2$ (Figure 5), which corresponds to a dissipation time-scale of approximately 1 day, shows good agreement with the PJ warming pattern. This is close to the original value of $\epsilon = 0.1$ used by Gill (1980). Correlations with the 700–200 hPa layer thickness anomalies in the PJ simulations are similar, but a bit weaker overall. The Gill model cannot capture the warming pattern in the lower to midtroposphere (700–400 hPa) well, because dissipative processes are weak at those levels (Bao *et al.*, 2022), and therefore the WTG assumption holds more accurately (Bao and Stevens, 2021). Therefore, the Gill model is best suited to reproduce the upper tropospheric warming at 400–150 hPa. For the case of $\epsilon_p \neq \epsilon_w$, a slightly higher correlation can be found for $\epsilon_p \approx 0.1$ and $\epsilon_w \approx 0.3$ (Figure 6b). Note that the correlation between SST anomalies and upper tropospheric warming anomalies (Figure 1) is only at 0.4, whereas some of the Gill simulations have correlations of almost 0.9, illustrating that the Gill model provides a much more accurate estimate for the warming pattern than simply inferring it from SSTs. Using mutual information (Datseris and Parltitz, 2022) as a measure of correlation, which also takes nonlinear, non-monotonic dependencies between two variables into account, yielded very similar results.

Because the dissipation terms have considerable influence on shaping the pattern, we investigate what processes might act to dissipate momentum in this magnitude. The momentum dissipation terms have been suggested to correspond to advection and eddy momentum flux (Lin *et al.*, 2008). We calculate horizontal advection of zonal

wind A :

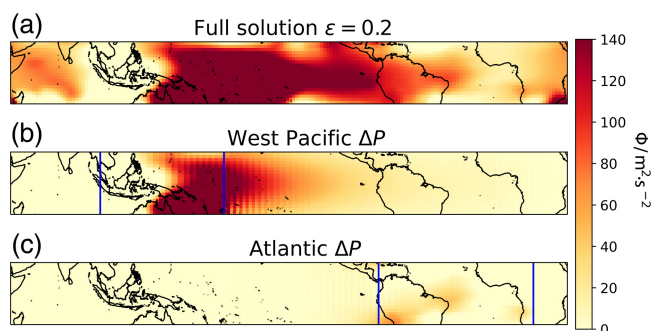
$$A = \overline{U} \frac{\partial \overline{U}}{\partial x} + \overline{V} \frac{\partial \overline{U}}{\partial y}, \quad (12)$$

where U and V are the zonal and meridional wind velocities respectively in the PJ simulations. The overline indicates monthly mean values. In addition, we calculate the horizontal eddy momentum fluxes of zonal wind E :

$$E = \frac{\partial \overline{U'U'}}{\partial x} + \frac{\partial \overline{U'V'}}{\partial y}, \quad (13)$$

and here the primes denote daily mean deviations from monthly mean values. We omit the contributions from vertical advection and eddy momentum fluxes because the vertical velocities are not available as output variable in the PJ simulations. Comparing the dissipation in the Gill model with A and E , Figure 7 shows that A in particular, but also E , has magnitudes similar to the dissipation term in the Gill model for $\epsilon_w = 0.1$. The patterns between the Gill model dissipation and A are similar in some regions, like the eastern Pacific or the Atlantic. In other regions the pattern is considerably different, which is likely because additional processes, like the convective momentum transport (Lin *et al.*, 2008) that are not included here, contribute to the dissipation term. Also, the rather simple dissipation term is limited in its ability to parametrise the spatial structure of these complex processes. It is noteworthy that A in particular is considerably stronger in the Atlantic than suggested by the momentum dissipation in the Gill model, which explains the spatially confined warming signal in the Atlantic compared with the Pacific in the PJ simulations. We conclude that horizontal advection and

FIGURE 8 Numerical Gill simulations forced by precipitation changes (a) over the whole Tropics, (b) only in the West Pacific (100–180° E, marked by blue lines), and (c) only in the Atlantic (–80° E to +20° E, marked by blue lines). All simulations are done with $\epsilon_p = \epsilon_w = 0.2$. [Colour figure can be viewed at wileyonlinelibrary.com]



eddy momentum flux contribute to shaping the warming pattern.

Finally, more idealised experiments that only use precipitation changes from one region as forcing can further illustrate the basins of influence that determine how far a convective heating signal is communicated before it dissipates. Figure 8 presents cases where the Gill model is only forced with precipitation changes in the West Pacific and Atlantic. The West Pacific forcing alone can explain a large part of the widespread Pacific warming, which is evocative of the Kelvin wave response east of the forcing in the idealised solution (Figure 4). However, the pattern in the Atlantic is not reproduced, illustrating that the signal dissipates before it can reach the Atlantic. In contrast, the Atlantic layer thickness changes can be reproduced quite well by the local precipitation changes. Thus, for $\epsilon = 0.2$, the basin of influence of western Pacific convection does not reach into the Atlantic (and vice versa). Dissipative processes are responsible for shaping these basins of influence, such that regional changes in convective heating can have regionally confined effects on the temperature pattern. This illustrates that the tropical mean upper tropospheric temperature is not controlled by convection in a single tropical region, but rather a spectrum of convective plumes across the Tropics.

4.2 | CMIP6

We now repeat the analysis for all CMIP6 models using the SSP585 simulations. For each CMIP6 model, the convective heating Q is calculated with the precipitation changes between the 2080–2099 and 2015–2034 periods and used as forcing for an ensemble of numerical Gill simulations with varying values for ϵ_p and ϵ_w . The correlation coefficient between the upper tropospheric layer thickness change from the respective CMIP6 model and all corresponding Gill simulations is given in Figure 9 for the December–February (DJF) season. Results for only using January precipitation or the June–August (JJA) season are overall similar and not shown in the interest of

conciseness. For every CMIP6 model except two in the DJF case, a corresponding Gill simulation with a layer thickness correlation coefficient higher than 0.5 exists, which we take as the threshold to indicate a skilful Gill simulation. In most instances, the $\epsilon = 0.1$ simulation (shown as an orange dot) appears at the upper end of the distribution. For annual means (not shown) the correlations are worse, although the Gill model is linear and the sum of the terms for individual seasons should be equivalent to the annual mean forcing. This suggests that the processes represented by the dissipation terms vary seasonally (Bao *et al.*, 2022), and thus an annual mean dissipation term is less skilful at describing the relevant mechanisms. Similar to the PJ results, the 700–200 hPa layer thickness shows smaller correlations, and for only about half of the CMIP6 models does a Gill simulation with a correlation larger than 0.5 exist (not shown).

4.3 | What are the optimal values for the dissipation time-scale and do they change under global warming?

We use the Gill simulations of the CMIP6 ensemble to assess which is the most skilful value for ϵ to simulate upper tropospheric warming (Figure 10). The values of ϵ_p that achieve the highest correlation are distributed around 0.05 (Figure 10a, corresponding to a dissipation time-scale of 5 days). The ϵ_w distribution centres around slightly larger values of 0.1 (Figure 10b, corresponding to a dissipation time-scale of 2 days). The JJA season shows similar optimal ϵ values that generally lie around $\epsilon = 0.1$ (not shown), but the distributions also show differences between the seasons, demonstrating the seasonality of the dissipative processes. Advection and eddy momentum flux have equivalent dissipation time-scales (Figure 7; (Lin *et al.*, 2008; Romps, 2014)) as the optimal ϵ_w values, illustrating that they are important for shaping the warming pattern in the CMIP6 models. In the case of ϵ_p , radiative cooling, which acts on a time-scale of a couple of days, seems represented with a realistic magnitude,

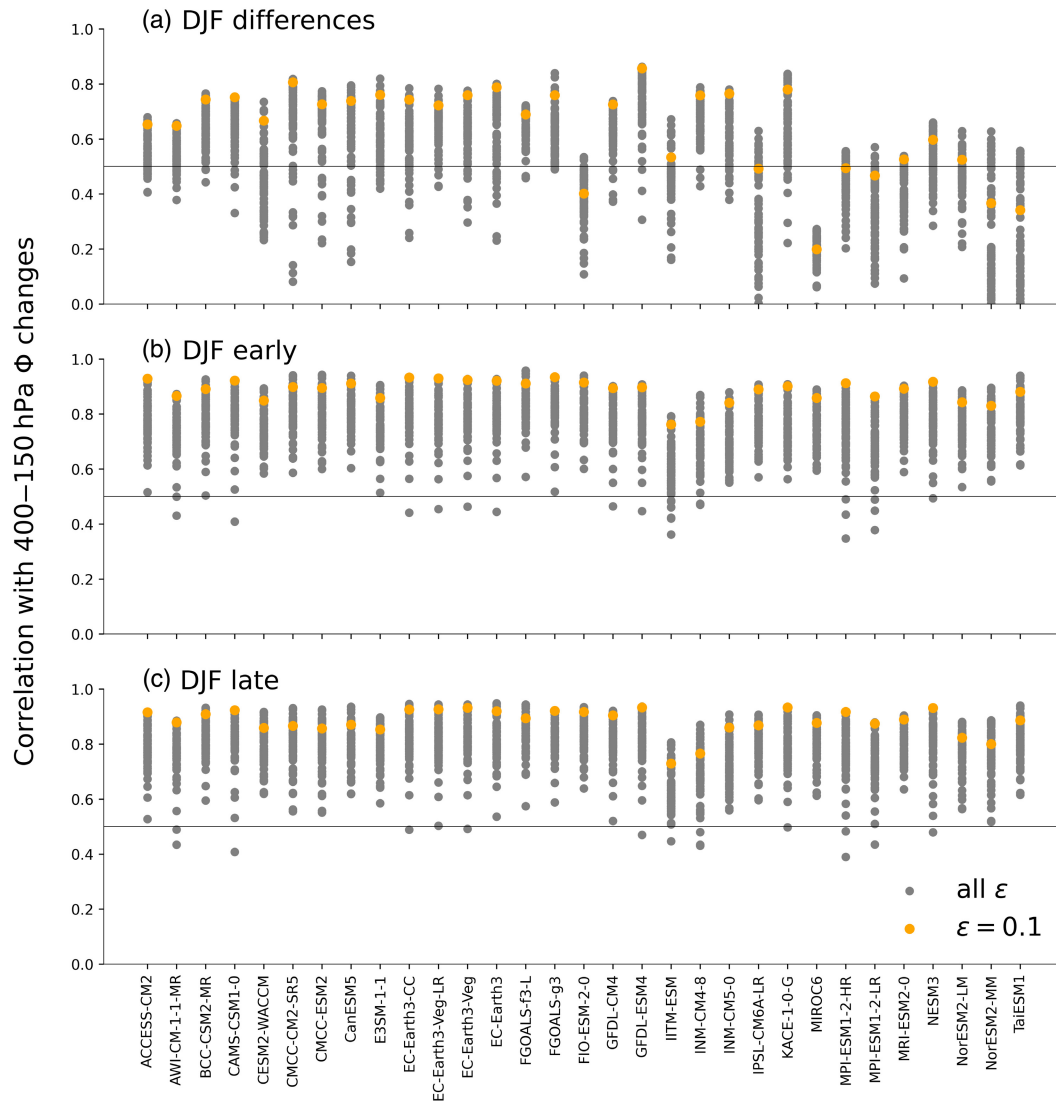


FIGURE 9 Correlation of Gill simulations for a range of ϵ_p and ϵ_w values with the 400–150 hPa layer thickness anomalies in every Coupled Model Intercomparison Project phase 6 SSP585 model (grey dots). The values for ϵ_p and ϵ_w range from 0 to 1.5, although some Gill simulations do not converge to steady state for small ϵ and, therefore, are not used. Orange dots show the simulations with $\epsilon_p = \epsilon_w = 0.1$. Correlations are calculated for 10°N – 20°S . DJF: December–February; JJA: June–August. [Colour figure can be viewed at wileyonlinelibrary.com]

although the range of optimal ϵ_p is quite large. Horizontal temperature advection, represented here through $\epsilon_p \Phi$, has also been shown to have a substantial contribution to the thermodynamic equation in some parts of the tropical upper troposphere (Bao *et al.*, 2022). We conclude that the original values of $\epsilon = 0.1$ (2 days) used by Gill (1980) are a good first estimate.

In the case of no thermal dissipation, $\epsilon_p = 0$, for almost all CMIP6 models there is no corresponding Gill simulation that converges to steady state (not shown). We also tested simulations for $\epsilon_p = 0$ that have a zonally compensated forcing, which has been interpreted as the WTG configuration of the Gill model (Bretherton and Sobel, 2003), because in this configuration the thermal dissipation is

implicitly included in Q and does not depend on Φ . In this case the simulations still usually only converge for $\epsilon_w \geq 0.1$. There is one CMIP6 model for which a corresponding Gill simulation in the WTG configuration during the DJF season shows the highest correlation (Figure 10a), and three models in the case of JJA.

The results presented so far are based on Gill simulations that are forced by the precipitation differences between a warm and a cold climate. This method is valid if one assumes that all terms in the Gill model are linear, and therefore additive. However, both α and ϵ might change under global warming, and therefore we investigate to what degree the assumption of invariance is valid.

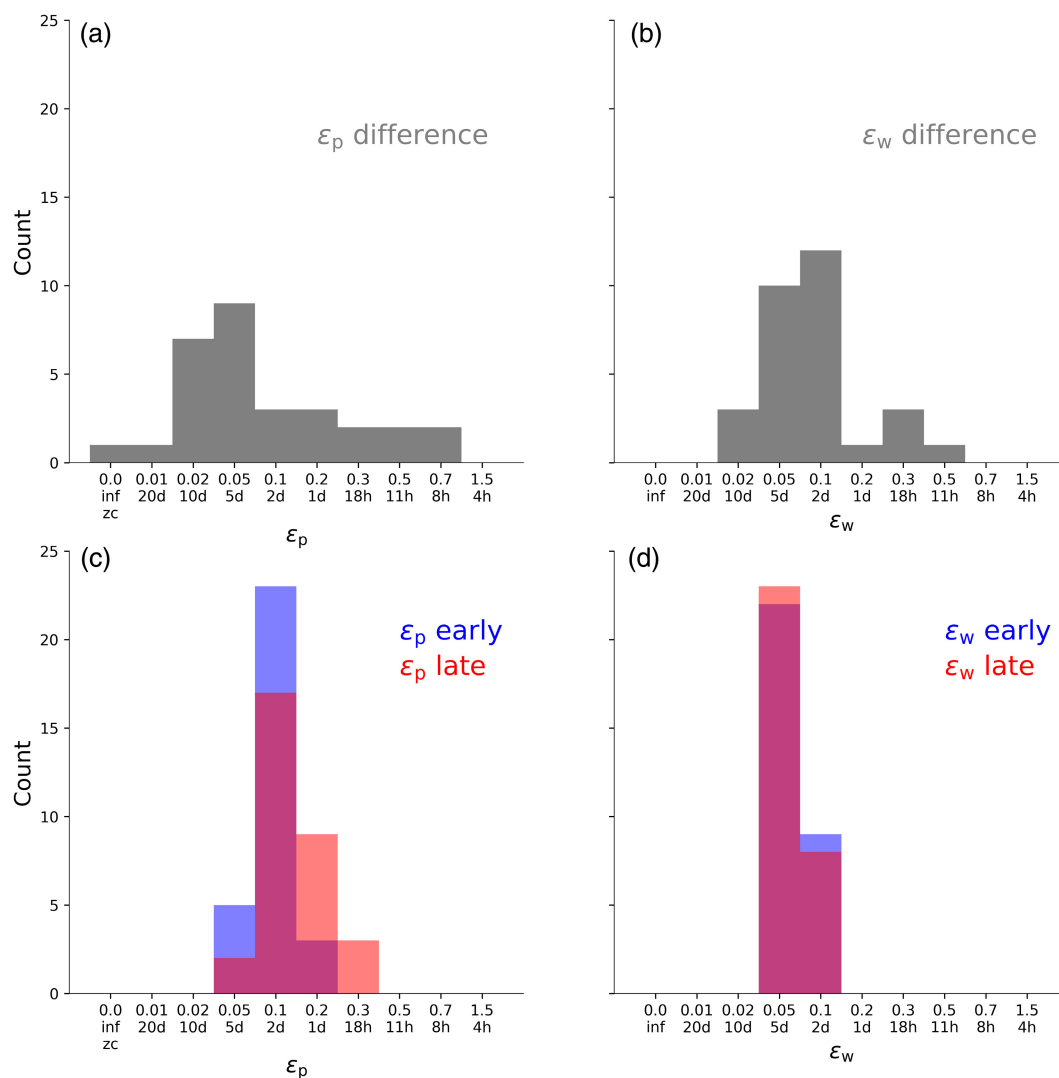


FIGURE 10 Histogram of dissipation values that yield the highest correlation. This plot counts the number of cases in which certain (a, c) ϵ_p and (b, d) ϵ_w values achieve the best correlation for every Coupled Model Intercomparison Project phase 6 model, given there is a Gill simulation that exceeds a correlation of 0.5. Results are shown for the December–February period. The dissipation is given in its non-dimensional value on the x -axis, as well as the corresponding dimensional dissipation time-scale (where d refers to day, h to hour, and inf to infinite time-scale). (a, b) Gill simulations forced by the precipitation differences that arise between the early (2015–2034) and late (2080–2099) periods; (c, d) Gill simulations forced by the mean precipitation from the early (2015–2034, blue) and late (2080–2099, red) periods. For the case $\epsilon_p = 0$, the forcing Q is zonally compensated (indicated by “ZC”), following Bretherton and Sobel (2003). [Colour figure can be viewed at wileyonlinelibrary.com]

To analyse the impact of changes in the dissipation terms, we perform individual Gill simulations that are forced by the precipitation fields from the cold and warm climate states of the PJ simulations. Figure 11 shows correlation coefficients between layer thickness in the PJ simulations and the Gill simulations individually for the cold (a) and warm (b) climates. While not completely identical, both cases are very similar and show the most skill for $0.06 < \epsilon_p < 0.2$ and $\epsilon_w \approx 0.1$. These values are overall very similar to the Gill simulation forced by precipitation differences (Figure 6b). However, it is notable that the optimal ϵ_w values shift to slightly larger values (from $\epsilon_w = 0.08$

to $\epsilon_w = 0.1$) in the warmer climate and the simulation forced by precipitation differences shows the most skill for $\epsilon_w \approx 0.3$ (Figure 6b). The overall skill of the Gill simulations, measured by the correlation coefficient, is slightly higher for the cases forced by the precipitation of the warm or the cold climate compared to the case forced by the precipitation differences. We conclude that the optimal dissipation terms change slightly in the warmer PJ simulation, nevertheless using the precipitation differences to simulate the warming pattern with invariant ϵ values is justified. As expected from the linearity of the Gill model, when subtracting the Gill model layer thickness in the cold

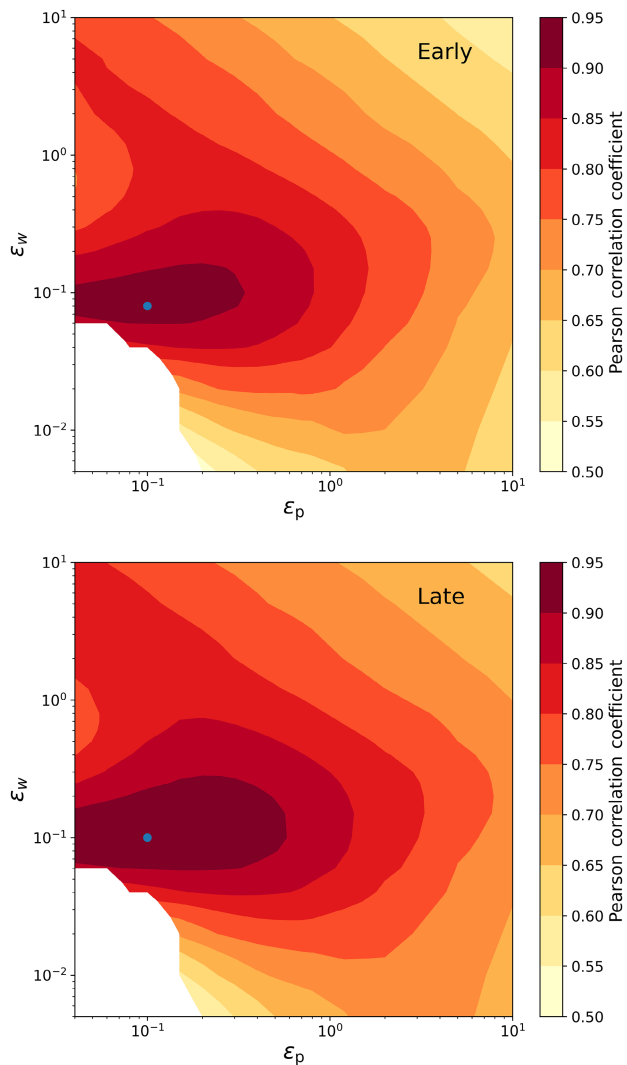


FIGURE 11 As Figure 6b, but for Gill simulations forced by the precipitation in the (a) early 21st century and (b) late 21st century. [Colour figure can be viewed at [wileyonlinelibrary.com](https://onlinelibrary.wiley.com)]

simulation from the warm simulation for constant ϵ , one obtains exactly the same solutions as the ones discussed in Section 4.1.

The assumption of unchanged dissipation terms does not hold equally well for all CMIP6 models, though. Using only the CMIP6 precipitation from the early (2015–2034) or late (2080–2099) period as forcing, the corresponding Gill simulations show very high skill in reproducing the mean layer thickness pattern (Figure 9b,c). These correlations are higher than the case forced by precipitation differences (Figure 9a). Is this because the optimal values for ϵ change with global warming? For ϵ_p the optimal value seems to shift to slightly larger values with warming (Figure 10c), whereas there is hardly any change for the momentum dissipation time-scale ϵ_w (Figure 10d). In simulations forced by precipitation differences (Figure 10a,b) the Gill simulations show a broader range of

optimal values for ϵ , whereas the distribution remains centred around a dissipation time-scale of 5 to 2 days. There is a better agreement between the Gill simulations forced by the mean precipitation and the Gill simulations forced by the precipitation differences for ϵ_w than for ϵ_p . Thus, the processes represented by ϵ_p seem to be more affected by global warming, and there are a few CMIP6 models where the assumption of constant ϵ_p is questionable. We conclude that the optimal momentum dissipation time-scale does not seem to change substantially for most CMIP6 models under global warming. Though the assumption of a constant thermal dissipation parameter ϵ_p does not always hold, the Gill model still reproduces the warming pattern decently for most CMIP6 models (Figure 9a). Overall, the optimal dissipation time-scales for individual models vary more between seasons than they do between the warm and cold climate, which is likely why Gill simulations forced by annual average precipitation perform worse. The results from the individual Gill simulations discussed here reinforce our claim that the realistic dissipation time-scale is indeed between 1 and 10 days.

The static stability increases with warming, which makes α around 18% larger based on calculations using values for the cold and warm PJ simulations. The strength of α determines gravity wave speeds in the Gill model, and indeed there is evidence that gravity wave speeds and Kelvin wave speeds increase in CMIP6 models with warming (Bartana *et al.*, 2023). We acknowledge that this is an important consideration for the tropospheric temperature pattern; but given various other assumptions (see Section 2) and the strong variations in ϵ throughout the experiments, the increase in static stability, and therefore α , is small in comparison. Therefore, investigating how changes in gravity- and Kelvin-wave speeds affect the tropospheric temperature pattern are beyond the scope of this study and remains an open question to address in future studies.

5 | DISCUSSION AND CONCLUSION

Climate model projections of tropical upper tropospheric warming, though broadly uniform, show horizontal differences of 2 K or more, which could have implications for different aspects of tropical circulation (Sohn *et al.*, 2016; Trabing *et al.*, 2019). We show that SST changes trigger both changes in the large-scale precipitation pattern and circulation, which in turn shape the upper tropospheric warming pattern. We demonstrate this causal mechanism by forcing a numerical Gill model with precipitation changes and thereby reproduce the different warming patterns in both storm-resolving and CMIP6 models. Thus,

the leading order balance that is responsible for the warming pattern is given by the Gill model. The dissipation term controls how localised the response to convective heating is and thereby determines a basin of influence. In particular, the advection and eddy momentum fluxes have strong enough equivalent dissipation time-scales to sustain layer thickness gradients at the Equator and shape the warming pattern. The optimal value of ϵ in most CMIP6 models corresponds to dissipation time-scales of 1–10 days. Even though the dissipation in the Gill model is a crude parametrisation for processes like advection, eddy momentum flux (Sardeshmukh and Held, 1984; Lin *et al.*, 2008), and radiative cooling, it is essential for reproducing the main features of the warming pattern, illustrating that these processes are important for shaping the tropospheric warming pattern. These results are robust over different types of climate models (storm-resolving or conventional climate models) and different time periods (JJA, DJF, or just January).

Though the overall signal is well reproduced by the simple Gill model, there are limitations regarding the assumption of the invariance of the parameters with warming, as discussed in Section 4.3. In addition, there is no vertical dimension, and thus the convective heating is assumed to be evenly distributed across the layer. However, some of the convective heating changes might be more relevant for the tropical midtroposphere and lower troposphere; in the Indian Ocean, for example, the 700–200 hPa layer thickness changes in the PJ simulations indicate a stronger relative increase compared with the 400–150 hPa case. This is also reproduced in the Gill simulations to some extent (the $\epsilon = 1.2$ case in Figure 5), suggesting a stronger influence of midlevel convection in this region. Furthermore, the processes represented by the dissipation vary horizontally across the domain, which could explain why some features of the warming pattern are more localised in some areas (like the Atlantic in the PJ simulations) and more “smeared out” (i.e., a less dissipated wave signal) in other areas. Adding more complexity, like using non-uniform dissipation terms or including an advection term, could improve results even further but defeats the purpose of understanding the leading order balance. For some CMIP6 models, the values for ϵ_w are slightly larger (i.e., represent shorter dissipation time-scales) compared with the results of Lin *et al.* (2008), but it is not clear whether this is due to the inadequacy of our method, due to biases in CMIP6 models, or due to biases in the reanalysis data used by Lin *et al.* (2008). The circulation produced by the Gill model also matches the climate models’ circulation changes well, although correlations are slightly lower than those of the layer thickness changes. Climate models often show jet-like anomalies of zonal wind in the tropical upper troposphere that are

related to extratropical geopotential changes (Rotstayn *et al.*, 2013), which the Gill model cannot capture. In addition, vertical momentum transport through convection acts as a torque and thereby can have substantial impacts on upper tropospheric circulation (Showman and Polvani, 2010; Shaw and Boos, 2012), which is likely not adequately represented by the dissipation parameters here.

Gill simulations using the WTG configuration of $\epsilon_p = 0$, with a zonally compensated forcing (Bretherton and Sobel, 2003), do not perform well overall. However, because these simulations only converge (i.e., reach a stable steady state) for high enough ϵ_w , they are only meaningful to some degree. In any case, the purpose of the WTG framework is not to study temperature gradients (or warming gradients) themselves, but instead facilitate the simulation and understanding of other aspects of tropical circulation (e.g., Bretherton and Sobel (2002)), and thus it is not surprising that this configuration might not work well. In fact, in the tropical upper troposphere, horizontal temperature advection can also substantially impact temperatures in some regions (Bao *et al.*, 2022), which would be represented here by $\epsilon_p \Phi$. The assumptions used to derive the shallow-water equations, and thereby also the Gill model, become increasingly justified for thinner layers, which means smaller values of α . However, thinner layers are not necessarily well represented by the Gill model, as demonstrated by the case of the 700–400 hPa layer (Figure 6a), although it is thinner ($\alpha \approx 2,300 \text{ m}^2 \cdot \text{s}^{-2}$) than the 400–150 hPa layer ($\alpha \approx 2,800 \text{ m}^2 \cdot \text{s}^{-2}$). This suggests that the temperature pattern in the lower troposphere to midtroposphere is well described by the WTG approximation, whereas the upper troposphere is better represented by the Gill model. A more extreme version of assuming temperature gradients are weak is to set the layer thickness gradients to zero in the momentum equations. In that case the winds quickly dissipate and the thermodynamic equation is left with the balance $\Phi \epsilon_p = Q$, which means that the warming pattern coincides with the pattern of forcing Q .

Finally, if the precipitation changes were mainly of thermodynamic nature, then the strongest warming would happen roughly over the existing convective hotspots and should be easy to predict. This can also be illustrated in the thermodynamic equation in the Gill model: If the circulation did not change, which means $u = v = 0$ in our configuration of the Gill model, and precipitation changes were purely related to thermodynamic processes, then the warming pattern Φ would be given directly by the forcing Q (assuming steady state): $\Phi \epsilon_p = Q$, where Q should be only derived from ΔP_{th} . This case results in a correlation of 0.03 between the Gill layer thickness and the layer thickness in the PJ simulations, illustrating the need to understand the coupling of precipitation

and circulation for the warming pattern. These dynamical precipitation changes are strongly influenced by the SST pattern, which in turn differs considerably across climate models, and consequently upper tropospheric warming patterns also differ across climate models. This makes the problem more complex but is in agreement with past studies that have related SSTs (and their coupling to convection) to mean upper tropospheric warming (Fueglistaler *et al.*, 2015; Tuel, 2019) and the local cooling in the upper tropospheric West Pacific in recent decades (Kamae *et al.*, 2015). The warming contrast between land and ocean surfaces could also affect the pattern of precipitation (He and Soden, 2017) and thereby modulate the upper tropospheric warming pattern. Though climate models still have considerable problems simulating realistic tropical SSTs and precipitation, with our study we demonstrate that, once climate models improve this aspect of tropical climate, projections of upper tropospheric warming patterns should also improve and become more consistent across different models.

AUTHOR CONTRIBUTIONS

P. Keil: conceptualization; formal analysis; investigation; methodology; software; visualization; writing – original draft; writing – review and editing. **H. Schmidt:** conceptualization; investigation; methodology; supervision; writing – review and editing. **B. Stevens:** conceptualization; methodology; supervision; writing – review and editing. **M. P. Byrne:** investigation; methodology; writing – review and editing. **H. Segura:** conceptualization; methodology; writing – review and editing. **D. Putrasahan:** data curation; methodology; software.

ACKNOWLEDGEMENTS

We would like to thank C. Stephan, J. Bao, G. Datsaris, and T. Birner for valuable discussion and feedback. In addition, we thank the reviewers for their comments. The research is supported by public funding to the Max Planck Society. H. Schmidt acknowledges support from the German Federal Ministry of Education and Research within the SOCTOC project of the ROMIC2 programme. Open Access funding enabled and organized by Projekt DEAL.

CONFLICT OF INTEREST STATEMENT

The authors declare no conflict of interest.

DATA AVAILABILITY STATEMENT

Code to run the numerical Gill model is available at https://github.com/pkeil7/numerical_gill. Code to reproduce analysis and figures is available at https://github.com/pkeil7/tropospheric_warming. CMIP6 data are available at DKRZ (<https://www.dkrz.de/de>) or

from the Earth System Grid Federation (ESGF) (<https://esgf-node.llnl.gov/projects/cmip6/>). The PJ simulations are available upon request to the corresponding author (paul.keil@mpimmet.mpg.de) or Dian Putrasahan (dian.putrasahan@mpimmet.mpg.de).

ORCID

P. Keil  <https://orcid.org/0000-0002-6502-4148>

B. Stevens  <https://orcid.org/0000-0003-3795-0475>

M. P. Byrne  <https://orcid.org/0000-0001-9019-3915>

REFERENCES

- Bao, J., Dixit, V. and Sherwood, S.C. (2022) Zonal temperature gradients in the tropical free troposphere. *Journal of Climate*, 35(24), 7937–7948.
- Bao, J. and Stevens, B. (2021) The elements of the thermodynamic structure of the tropical atmosphere. *Journal of the Meteorological Society of Japan Ser. II*, 99(6), 1483–1499.
- Bartana, H., Garfinkel, C.I., Shamir, O. and Rao, J. (2023) Projected future changes in equatorial wave spectrum in cmip6. *Climate Dynamics*, 60, 3277–3289.
- Bayr, T., Dommenges, D., Martin, T. and Power, S.B. (2014) The eastward shift of the Walker circulation in response to global warming and its relationship to ENSO variability. *Climate Dynamics*, 43, 2747–2763.
- Bony, S., Bellon, G., Klocke, D., Sherwood, S., Fermepin, S. and Denvil, S. (2013) Robust direct effect of carbon dioxide on tropical circulation and regional precipitation. *Nature Geoscience*, 6, 447–451.
- Bretherton, C.S. and Smolarkiewicz, P.K. (1989) Gravity waves, compensating subsidence and detrainment around cumulus clouds. *Journal of the Atmospheric Sciences*, 46, 740–759.
- Bretherton, C.S. and Sobel, A.H. (2002) A simple model of a convectively coupled walker circulation using the weak temperature gradient approximation. *Journal of Climate*, 15, 2907–2920.
- Bretherton, C.S. and Sobel, A.H. (2003) The Gill model and the weak temperature gradient approximation. *Journal of the Atmospheric Sciences*, 60, 451–460.
- Datsaris, G. and Parltitz, U. (2022) *Nonlinear Dynamics: A Concise Introduction Interlaced with Code*. Cham, Switzerland: Springer International Publishing.
- Dias, P.S., Schubert, W.H. and DeMaria, M. (1983) Large-scale response of the tropical atmosphere to transient convection. *Journal of the Atmospheric Sciences*, 40, 2689–2707.
- Elbaum, E., Garfinkel, C.I., Adam, O., Morin, E., Rostkier-Edelstein, D. and Dayan, U. (2022) Uncertainty in projected changes in precipitation minus evaporation: dominant role of dynamic circulation changes and weak role for thermodynamic changes. *Geophysical Research Letters*, 49, e2022GL097725 <https://agupubs.onlinelibrary.wiley.com/doi/abs/10.1029/2022GL097725>.
- Emanuel, K.A., David Neelin, J. and Bretherton, C.S. (1994) On large-scale circulations in convecting atmospheres. *Quarterly Journal of the Royal Meteorological Society*, 120, 1111–1143.
- Eyring, V., Bony, S., Meehl, G.A., Senior, C.A., Stevens, B., Stouffer, R.J. and Taylor, K.E. (2016) Overview of the coupled model Intercomparison project phase 6 (CMIP6) experimental design and organization. *Geoscientific Model Development*, 9, 1937–1958.

- Fiedler, S., Crueger, T., D'Agostino, R., Peters, K., Becker, T., Leutwyler, D., Paccini, L., Burdanowitz, J., Buehler, S.A. and Cortes, A.U. (2020) Simulated tropical precipitation assessed across three major phases of the coupled model intercomparison project (cmip). *Monthly Weather Review*, 148, 3653–3680.
- Fueglistaler, S., Radley, C. and Held, I.M. (2015) The distribution of precipitation and the spread in tropical upper tropospheric temperature trends in CMIP5/AMIP simulations. *Geophysical Research Letters*, 42, 6000–6007.
- Gill, A.E. (1980) Some simple solutions for heat?Induced tropical circulation. *Quarterly Journal of the Royal Meteorological Society*, 106, 447–462.
- Gill, A.E. (1982) Studies of moisture effects in simple atmospheric models: the stable case. *Geophysical & Astrophysical Fluid Dynamics*, 19, 119–152.
- Gutjahr, O., Putrasahan, D., Lohmann, K., Jungclaus, J.H., von Storch, J.-S., Brüggemann, N., Haak, H. and Stössel, A. (2019) Max planck institute earth system model (mpi-esm1. 2) for the high-resolution model intercomparison project (highresmp). *Geoscientific Model Development*, 12, 3241–3281.
- He, J. and Soden, B.J. (2017) A re-examination of the projected subtropical precipitation decline. *Nature Climate Change*, 7, 53–57.
- Held, I.M. and Soden, B.J. (2006) Robust responses of the hydrological cycle to global warming. *Journal of Climate*, 19, 5686–5699.
- Hohenegger, C., Korn, P., Linardakis, L., Redler, R., Schnur, R., Adamidis, P., Bao, J., Bastin, S., Behraves, M., Bergemann, M., Biercamp, J., Bockelmann, H., Brokopf, R., Bröggemann, N., Casaroli, L., Chagini, F., Datsieris, G., Esch, M., George, G., Giorgetta, M., Gutjahr, O., Haak, H., Hanke, M., Ilyina, T., Jahns, T., Jungclaus, J., Kern, M., Klocke, D., Kluft, L., Kölling, T., Kornblueh, L., Kosukhin, S., Kroll, C., Lee, J., Mauritsen, T., Mehlmann, C., Mieslinger, T., Naumann, A.K., Paccini, L., Peinado, A., Praturi, D.S., Putrasahan, D., Rast, S., Riddick, T., Roeber, N., Schmidt, H., Schulzweida, U., Schötte, F., Segura, H., Shevchenko, R., Singh, V., Specht, M., Stephan, C.C., von Storch, J.-S., Vogel, R., Wengel, C., Winkler, M., Ziemann, F., Marotzke, J. and Stevens, B. (2023) ICON-Sapphire: simulating the components of the Earth system and their interactions at kilometer and subkilometer scales. *Geoscientific Model Development*, 16, 779–811. <https://doi.org/10.5194/gmd-16-779-2023>.
- Hohenegger, C. and Stevens, B. (2013) Preconditioning deep convection with cumulus congestus. *Journal of the Atmospheric Sciences*, 70, 448–464.
- Holton, J. and Hakim, G. (2013) *An Introduction to Dynamic Meteorology*. Waltham, MA: Academic Press.
- Kamae, Y., Shiogama, H., Watanabe, M., Ishii, M., Ueda, H. and Kimoto, M. (2015) Recent slowdown of tropical upper tropospheric warming associated with Pacific climate variability. *Geophysical Research Letters*, 42, 2995–3003.
- Lau, K.-M. and Lim, H. (1982) Thermally driven motions in an equatorial β -plane: Hadley and walker circulations during the winter monsoon. *Monthly Weather Review*, 110, 336–353.
- Lin, J.L., Mapes, B.E. and Han, W. (2008) What are the sources of mechanical damping in Matsuno-Gill-type models? *Journal of Climate*, 21, 165–179.
- Lindzen, R.S. and Nigam, S. (1987) On the role of sea surface temperature gradients in forcing low-level winds and convergence in the tropics. *Journal of Atmospheric Sciences*, 44, 2418–2436.
- Matsuno, T. (1966) Quasi-geostrophic motions in the equatorial area. *Journal of the Meteorological Society of Japan. Ser. II*, 44, 25–43.
- O'Neill, B.C., Tebaldi, C., Van Vuuren, D.P., Eyring, V., Friedlingstein, P., Hurtt, G., Knutti, R., Kriegler, E., Lamarque, J.-F. and Lowe, J. (2016) The scenario model intercomparison project (scenariomip) for cmip6. *Geoscientific Model Development*, 9, 3461–3482.
- Po-Chedley, S., Santer, B.D., Fueglistaler, S., Zelinka, M.D., Cameron-Smith, P.J., Painter, J.F. and Fu, Q. (2021) Natural variability contributes to model-satellite differences in tropical tropospheric warming. *Proceedings of the National Academy of Sciences of the United States of America*, 118, 1–7.
- Putrasahan, D., Gutjahr, O., Haak, H., Jungclaus, J.H., Lohmann, K., Roberts, M. and von Storch, J.-S. (2021) Effect of resolving ocean eddies on the transient response of global mean surface temperature to abrupt 4xco2 forcing. *Geophysical Research Letters*, 48, e2020GL092049.
- Rodwell, M.J. and Hoskins, B.J. (1996) Monsoons and the dynamics of deserts. *Quarterly Journal of the Royal Meteorological Society*, 122, 1385–1404.
- Romps, D.M. (2014) Rayleigh damping in the free troposphere. *Journal of the Atmospheric Sciences*, 71, 553–565.
- Rotstayn, L., Collier, M.A., Jeffrey, S.J., Kidston, J., Syktus, J. and Wong, K. (2013) Anthropogenic effects on the subtropical jet in the southern hemisphere: aerosols versus long-lived greenhouse gases. *Environmental Research Letters*, 8, 014030.
- Santer, B.D., Solomon, S., Pallotta, G., Mears, C., Po-Chedley, S., Fu, Q., Wentz, F., Zou, C.Z., Painter, J., Cvijanovic, I. and Bonfils, C. (2017) Comparing tropospheric warming in climate models and satellite data. *Journal of Climate*, 30, 373–392.
- Santer, B.D., Wigley, T.M., Mears, C., Wentz, F.J., Klein, S.A., Seidel, D.J., Taylor, K.E., Thorne, P.W., Wehner, M.F., Gleckler, P.J., Boyle, J.S., Collins, W.D., Dixon, K.W., Doutriaux, C., Free, M., Fu, Q., Hansen, J.E., Jones, C.S., Ruedy, R., Karl, T.R., Lanzante, J.R., Meehl, C.A., Ramaswamy, V., Russell, C. and Schmidt, C.A. (2005) Atmospheric science: amplification of surface temperature trends and variability in the tropical atmosphere. *Science*, 309, 1551–1556.
- Sardeshmukh, P.D. and Held, I.M. (1984) The vorticity balance in the tropical upper troposphere of a general circulation model. *Journal of the Atmospheric Sciences*, 41, 768–778.
- Seager, R., Naik, N. and Vecchi, G.A. (2010) Thermodynamic and dynamic mechanisms for large-scale changes in the hydrological cycle in response to global warming. *Journal of Climate*, 23, 4651–4668.
- Shaw, T.A. and Boos, W.R. (2012) The tropospheric response to tropical and subtropical zonally asymmetric torques: analytical and idealized numerical model results. *Journal of the Atmospheric Sciences*, 69, 214–235.
- Showman, A.P. and Polvani, L.M. (2010) The Matsuno-Gill model and equatorial superrotation. *Geophysical Research Letters*, 37, L18811. <https://doi.org/10.1029/2010GL044343>.
- Sobel, A.H. and Bretherton, C.S. (2000) Modeling tropical precipitation in a single column. *Journal of Climate*, 13, 4378–4392.
- Sobel, A.H., Nilsson, J. and Polvani, L.M. (2001) The weak temperature gradient approximation and balanced tropical moisture waves. *Journal of the Atmospheric Sciences*, 58, 3650–3665.
- Sohn, B.J., Lee, S., Chung, E.S. and Song, H.J. (2016) The role of the dry static stability for the recent change in the Pacific Walker circulation. *Journal of Climate*, 29, 2765–2779.
- Stevens, B., Acquistapace, C., Hansen, A., Heinze, R., Klinger, C., Klocke, D., Rybka, H., Schubotz, W., Windmiller, J., Adamidis, P., Arka, I., Barlakas, V., Biercamp, J., Brueck, M., Brune, S., Buehler,

S.A., Burkhardt, U., Cioni, G., Costa-Surós, M., Crewell, S., Crüger, T., Deneke, H., Friederichs, P., Henken, C.C., Hohenegger, C., Jacob, M., Jakob, F., Kalthoff, N., Köhler, M., van Laar, T.W., Li, P., Löhnert, U., Macke, A., Madenach, N., Mayer, B., Nam, C., Naumann, A.K., Peters, K., Poll, S., Quaas, J., Röber, N., Rochetin, N., Scheck, L., Schemann, V., Schnitt, S., Seifert, A., Senf, F., Shapkalijevski, M., Simmer, C., Singh, S., Sourdeval, O., Spickermann, D., Strandgren, J., Tessiot, O., Vercauteren, N., Vial, J., Voigt, A. and Zängl, G. (2020) The added value of large-eddy and storm-resolving models for simulating clouds and precipitation. *Journal of the Meteorological Society of Japan*, 98, 395–435.

Trabing, B.C., Bell, M.M. and Brown, B.R. (2019) Impacts of radiation and upper-tropospheric temperatures on tropical cyclone structure and intensity. *Journal of the Atmospheric Sciences*, 76, 135–153.

Tuel, A. (2019) Explaining differences between recent model and satellite tropospheric warming rates with tropical SSTs. *Geophysical Research Letters*, 46, 9023–9030.

Webster, P.J. (1972) Response of the tropical atmosphere to local, steady forcing. *Monthly Weather Review*, 100, 518–541.

Wu, G., He, B., Liu, Y., Bao, Q. and Ren, R. (2015) Location and variation of the summertime upper-troposphere temperature maximum over South Asia. *Climate Dynamics*, 45, 2757–2774. <https://doi.org/10.1007/s00382-015-2506-4>.

Yang, D., Zhou, W. and Seidel, S.D. (2022) Substantial influence of vapour buoyancy on tropospheric air temperature and subtropical cloud. *Nature Geoscience*, 15, 781–788.

How to cite this article: Keil, P., Schmidt, H., Stevens, B., Byrne, M.P., Segura, H. & Putrasahan, D. (2023) Tropical tropospheric warming pattern explained by shifts in convective heating in the Matsuno–Gill model. *Quarterly Journal of the Royal Meteorological Society*, 1–18. Available from: <https://doi.org/10.1002/qj.4526>

APPENDIX

Derivation of thermodynamic equation

We start with the thermodynamic equation in pressure coordinates (e.g., Holton and Hakim (2013)), but ignore horizontal temperature advection:

$$\frac{\partial T}{\partial t} + wT \frac{\partial \ln(\theta)}{\partial p} = \bar{Q}, \quad (\text{A1})$$

where T is the temperature, w is the vertical pressure velocity, θ is potential temperature, p is the pressure, and \bar{Q} is the heating rate. With $\partial\Phi/\partial p = -1/\rho$ and $p = \rho RT$, where ρ is the density and R is the gas constant, one obtains

$$-\frac{\partial}{\partial t} \frac{\partial \Phi}{\partial p} - w \frac{\partial \Phi}{\partial p} \frac{\partial \ln(\theta)}{\partial p} = \frac{R\bar{Q}}{p}. \quad (\text{A2})$$

We evaluate this equation on a set of vertical layers (typically $p_0 = 0$ hPa, $p_1 = 250$ hPa, $p_2 = 500$ hPa, $p_3 = 750$ hPa, $p_4 = 1,000$ hPa), where Φ , u , and v are defined on p_1 and p_3 , and w is defined on p_0 , p_2 , and p_4 . Assuming that the stability parameter

$$S = \frac{\partial \Phi}{\partial p} \frac{\partial \ln(\theta)}{\partial p}$$

and the heating rate \bar{Q} are vertically constant, Equation (A2) can be vertically integrated. Using the corresponding subscripts for each pressure layer one obtains

$$-\frac{\partial(\Phi_1 - \Phi_3)}{\partial t} - w_2 S(p_1 - p_3) = R\bar{Q} \ln\left(\frac{p_1}{p_3}\right). \quad (\text{A3})$$

We use the continuity equation

$$\nabla \cdot \mathbf{v} = -\frac{\partial w}{\partial p} \quad (\text{A4})$$

and assume $w_0 = w_4 = 0$ to obtain

$$\nabla \cdot \mathbf{v}_1 = \frac{w_2}{p_0 - p_2}; \quad \nabla \cdot \mathbf{v}_3 = -\frac{w_2}{p_2 - p_4}. \quad (\text{A5})$$

This can be used to derive an expression for w_2 :

$$w_2 = -\frac{\nabla \cdot (\mathbf{v}_3 - \mathbf{v}_1)}{\frac{1}{p_2 - p_4} + \frac{1}{p_0 - p_2}}, \quad (\text{A6})$$

which we substitute into Equation (A3) to get the final thermodynamic equation:

$$\frac{\partial \Phi_d}{\partial t} + Sa \left(\frac{\partial u_d}{\partial x} + \frac{\partial v_d}{\partial y} \right) = R\bar{Q} \ln\left(\frac{p_3}{p_1}\right), \quad (\text{A7})$$

where we define the layer thickness between the first and the third layer $\Phi_d = \Phi_1 - \Phi_3$ and the wind shear $u_d = u_1 - u_3$ and $v_d = v_1 - v_3$. These subscripts are dropped in the main part of the article. The parameter a is related to the chosen pressure levels:

$$a = \frac{p_1 - p_3}{\frac{1}{p_2 - p_4} + \frac{1}{p_0 - p_2}}, \quad (\text{A8})$$

which reduces to $a = (p_1 - p_3)^2/2$ for the case of equidistant layers. If not otherwise stated, we use $p_0 = 0$ hPa, $p_1 = 150$ hPa, $p_2 = 275$ hPa, $p_3 = 400$ hPa, and $p_4 = 1,000$ hPa, because our main focus is on the upper troposphere. For convenience, we use $p_t = p_1$ and $p_b = p_3$ in the main text.